Author Manuscript

Author Manuscript

Author Manuscript

Author Manuscript

HHS Public Access

Author manuscript

Nucl Med Biol. Author manuscript; available in PMC 2024 July 19.

Published in final edited form as:

Nucl Med Biol. 2023 ; 122-123: 108368. doi:10.1016/j.nucmedbio.2023.108368.

Preclinical studies of a PARP targeted, Meitner-Auger emitting, theranostic radiopharmaceutical for metastatic ovarian cancer

SLV Hoffman[1], **JC Mixdorf**[1], **O Kwon**[1], **TR Johnson**[1], **M Makvandi**[2], **H Lee**[2], **E Aluicio-Sarduy**[1], **TE Barnhart**[1], **JJ Jeffery**[3], **MS Patankar**[4], **JW Enge**[1,5], **BP Bednarz**[1], **PA Ellison**[1,*]

[1]Department of Medical Physics, University of Wisconsin—Madison, Madison, WI, USA

[2]Department of Radiology, University of Pennsylvania, Philadelphia, PA, USA

[3]University of Wisconsin Carbone Cancer Center, Madison, WI, USA

[4]Department of Obstetrics and Gynecology, University of Wisconsin—Madison, Madison, WI, USA

[5]Department of Radiology, University of Wisconsin—Madison, Madison, WI, USA

Abstract

Advanced ovarian cancer currently has few therapeutic options. Poly(ADP-ribose) polymerase (PARP) inhibitors bind to nuclear PARP and trap the protein-inhibitor complex to DNA. This work investigates a theranostic PARP inhibitor for targeted radiopharmaceutical therapy of ovarian cancer *in vitro* and PET imaging of healthy mice *in vivo*.

Methods: [^{77}Br]RD1 was synthesized and assessed for pharmacokinetics and cytotoxicity in human and murine ovarian cancer cell lines. [^{76}Br]RD1 biodistribution and organ uptake in healthy mice were quantified through longitudinal PET/CT imaging and *ex vivo* radioactivity measurements. Organ-level dosimetry following [$^{76/77}$Br]RD1 administration was calculated using RAPID, an in-house platform for absorbed dose in mice, and OLINDA for equivalent and effective dose in human.

Results: The maximum specific binding (B_{max}), equilibrium dissociation constant (K_d), and nonspecific binding slope (NS) were calculated for each cell line. These values were used to calculate the cell specific activity uptake for cell viability studies. The half maximal effective concentration (EC_{50}) was measured as 0.17 (95% CI: 0.13–0.24) nM and 0.46 (0.13–0.24) nM

*Corresponding author email: paellison@wisc.edu.

Publisher's Disclaimer: This is a PDF file of an unedited manuscript that has been accepted for publication. As a service to our customers we are providing this early version of the manuscript. The manuscript will undergo copyediting, typesetting, and review of the resulting proof before it is published in its final form. Please note that during the production process errors may be discovered which could affect the content, and all legal disclaimers that apply to the journal pertain.

Declaration of competing interest

The authors have no competing interests to report.

Declaration of interests

Preclinical studies of a PARP targeted, Meitner-Auger emitting, theranostic radiopharmaceutical for metastatic ovarian cancer. SLV Hoffman, JC Mixdorf, O Kwon, TR Johnson, M Makvandi, H Lee, E Aluicio-Sarduy, TE Barnhart, JJ Jeffery, MS Patankar, JW Engle, BP Bednarz, and PA Ellison

The authors declare that they have no known competing financial interests or personal relationships that could have appeared to influence the work reported in this paper.

Author Manuscript Author Manuscript Author Manuscript Author Manuscript

for PARP(+) and PARP(−) expressing cell lines, respectively. The EC_{50} was 0.27 (0.21–0.36) nM and 0.30 (0.22–0.41) nM for BRCA1(−) and BRCA1(+) expressing cell lines, respectively. When measuring the EC_{50} as a function of cellular activity uptake and nuclear dose, the EC_{50} ranges from 0.020–0.039 Bq/cell and 3.3–9.2 Gy, respectively. Excretion through the hepatobiliary and renal pathways were observed in mice, with liver uptake of 2.3±0.4 %ID/g after 48 h, contributing to estimated absorbed dose values in mice of 19.3±0.3 mGy/MBq and 290±10 mGy/MBq for [^{77}Br]RD1 and [^{76}Br]RD1, respectively.

Conclusion: [^{77}Br]RD1 cytotoxicity was dependent on PARP expression and independent of BRCA1 status. The *in vitro* results suggest that [^{77}Br]RD1 cytotoxicity is driven by the targeted Meitner-Auger electron (MAe) radiotherapeutic effect of the agent. Further studies investigating the theranostic potential, organ dose, and tumor uptake of [$^{76/77}$Br]RD1 are warranted.

Graphical Abstract

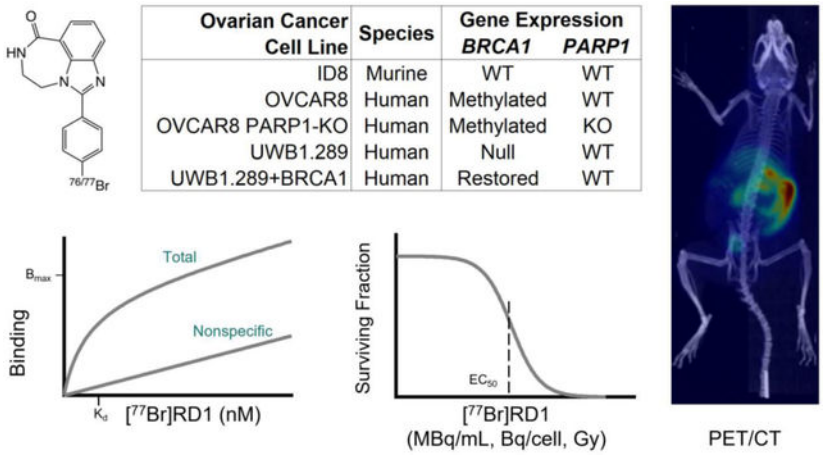

Keywords

bromine-77; bromine-76; Meitner-Auger radionuclide therapy; positron emission tomography; PARP-1 inhibitor; theranostic; ovarian cancer therapy

1. Introduction

An estimated 20,000 new cases of ovarian cancer will be diagnosed in 2023 with approximately 50% of patients presenting with distant-staged disease [1]. Upon metastasis of ovarian cancer, patients have a 5-year relative survival rate of 31%, only a 1–3% increase over the last 20 years [1], [2]. The current standard of care for advanced ovarian cancer includes cytoreductive surgery and platinum-based chemotherapy with curative intent [3]. Platinum-based chemotherapy drugs are known for their lack of selectivity, high systemic toxicity, and drug resistance [4]. Patients may have good initial response to this treatment, but approximately 75% of patients with advanced stage ovarian cancer will relapse, requiring further chemotherapy treatments. Furthermore, 30% of these patients will develop chemotherapy drug resistance, at which point, treatment shifts from curative intent to maximizing quality of life [5].

Author Manuscript Author Manuscript Author Manuscript Author Manuscript

Comprehensive molecular characterization of epithelial ovarian cancer (EOC) and especially high-grade serous ovarian cancer demonstrated an over-representation of *BRCA1/2* pathogenic variants [6]. This demonstrates the importance of double strand DNA repair pathways, such as homologous recombination (HR), with further studies confirming that dysfunction in this pathway leads to a higher risk of development of EOC [7], [8]. Drugs targeting the DNA damage response systems provides an opportunity to target this advanced disease for patients who otherwise have poor prognosis and few treatment options. Poly(ADP-ribose) polymerase (PARP) enzymes are nuclear proteins with a critical role in DNA damage response. PARP inhibitors exploit synthetic lethality through single-strand break and double-strand break repair pathways, specifically the HR impaired pathway [9]–[12]. FDA approved PARP inhibitors olaparib, rucaparib, and talazoparib trap the PARP-drug complex nanometers from target DNA [13] making them viable diagnostic and therapeutic radiopharmaceutical candidates in cancers with PARP expression [14].

The use of positron emission tomography (PET) imaging to assess physiologic PARP expression in patients has been established as a noninvasive imaging tool [14]. Two ^{18}F-labeled PARP inhibitors are in the process of being translated from preclinical research to clinical PET application [15]–[17]. The first agent, [^{18}F]FTT, is a rucaparib analog which has shown potential for imaging PARP [18]. Multiple studies have demonstrated [^{18}F]FTT's efficacy in preclinical models, and human trials are currently underway [16], [19]. The second agent is an olaparib analog, [^{18}F]PARPi, that targets PARP and has shown promise in imaging breast, ovarian and brain cancers [17], [20]. [^{18}F]PARPi has also been shown to have potential in imaging other DNA damage response pathways, including DNA-PK, ATR, and ATM [21] and is currently undergoing clinical trials investigating its potential as a diagnostic tool for cancer. Additional ^{18}F-labeled isotopologues that have been preclinically investigated include [^{18}F]rucaparib [22], [23], [^{18}F]talazoparib [24], [25], and [^{18}F]olaparib [26], [27].

PARP has been targeted in radiopharmaceutical therapy using olaparib- and rucaparib-derived agents labeled with various radionuclides, including β^- emitter ^{131}I [28], alpha-emitter ^{211}At [29]–[31], and Meitner-Auger electron (MAe) emitters ^{125}I [32]–[35], ^{123}I [28], [35] and ^{77}Br [36]. These preclinical studies have investigated responses in ovarian cancer [35] as well as glioblastoma [28], [37], [38], neuroblastoma [32], colon [33], breast [34], prostate cancers [36]. The biological mechanism of PARP that brings its inhibitors within nanometers of DNA is well suited for use with the low energy (eV–keV), short range (0.001–100 μm), and high linear energy transfer (LET, 1–23 keV/μm) of MAe [39]. *In vitro* cell cytotoxicity studies show MAe PARP inhibitors to be highly cytotoxic across several cancer cell lines [32], [34], [35], [37], [40], and tumor-bearing mice treated with MAe PARP inhibitors were observed to have prolonged survival *in vivo* [28], [33], [36]. Higher cytotoxicity was observed compared to radioinert PARP inhibitors with no dependence on *BRCA1* expression [35]. These results show promising radiotherapeutic potential that warrants further preclinical and clinical investigation across a multitude of cancers.

Rucaparib is FDA approved for both treatment and maintenance therapy of ovarian cancer [41] and a derivative of this molecule was investigated as a theranostic radiopharmaceutical labeled with MAe-emitting ^{77}Br ($t_{1/2} = 57$h, 6–7 MAe per decay) [42] and positron emitting

Author Manuscript Author Manuscript Author Manuscript Author Manuscript

^{76}Br ($t_{1/2}$ = 16 .2h, 55%β^+). The short-range MAe from ^{77}Br deposits their energy locally [43], providing low dose to off-target cells. Bromine forms a more stable bond with carbon compared with iodine, resulting in less dehalogenation of radiopharmaceuticals *in vivo*. Additionally, unlike radioiodine, free radiobromine does not accumulate in the thyroid, diffusing evenly throughout the body with only the stomach reaching higher uptake than blood [44], [45]. The PARP inhibitor mechanism provides a biological approach to localize the radioactive drug to the DNA. The imaging analog, labeled with ^{76}Br, allows for noninvasive *in vivo* PET imaging [46], [47] of radiopharmaceutical biodistribution. This study examines the *in vitro* radiopharmacology and toxicology of rucaparib derived [^{77}Br]RD1. Additionally, it investigated the potential for *in vivo* PET imaging of its diagnostic analog, [^{76}Br]RD1, in healthy mice.

2. Materials and Methods

2.1 Radiosynthesis of [$^{76/77}$Br]RD1

Production of $^{76/77}$Br and [$^{76/77}$Br]RD1 synthesis and quality control were performed according to published procedures as detailed in the supplementary methods [48], [49]. Proton irradiation of Co$^{76/77}$Se yielded $^{76/77}$Br which was isolated via dry distillation. [$^{76/77}$Br]RD1 was synthesized by Cu-mediated bromo deborylation chemistry of a boronic acid pinacol ester precursor (Figure 1). [$^{76/77}$Br]RD1 was isolated by preparative high performance liquid chromatography (HPLC), and subsequently formulated for *in vitro* and *in vivo* studies in sterile phosphate buffered saline (PBS). Molar activity and radiochemical purity of [$^{76/77}$Br]RD1 were evaluated by analytical HPLC and autoradiography-visualized thin layer chromatography (radioTLC, Fig. S1–2) with methods further described in the supplementary materials.

2.2 Cell Culture

Murine ID8 ovarian cancer cells were gifted from Dr. Katherine Roby (University of Kansas, KS) and maintained in Dulbecco's modified Eagle's medium with 4.5 g/L glucose, L-glutamine, and sodium pyruvate (Corning) supplemented with 5% fetal bovine serum (FBS, Corning), 1% penicillin-streptomycin (Corning) and 0.2% 500X insulin-transferrin-selenium supplement (BioWhittiker). OVCAR8 and OVCAR8 PARP1-KO G1 (isogenic pair to OVCAR8 with PARP1 knocked out, [50]) human ovarian cancer cells were maintained in RPMI-1640 medium (Gibco) supplemented with 10% FBS and 1% penicillin-streptomycin. OVCAR8 PARP1-KO G1 had an additional 2 μg/mL puromycin (Gibco) added to the medium. UWB1.289 and UWB1.289+BRCA1 (isogenic pair to UWB1.289 with BRCA1 restored) human ovarian cancer cells were purchased from American Type Culture Collection and maintained in 1:1 RPMI-1640 (Gibco) and mammary epithelial growth medium (Lonza) supplemented with 3% FBS. UWB1.289+BRCA1 media also had 200 μg/mL Geneticin selective antibiotic (G418 Sulfate, Gibco). All cells were cultured in a humidified environment at 37°C and 5% CO_2.

2.3 [^{77}Br]RD1 in vitro binding assays

All cell lines were grown in clear, sterile, tissue-culture (TC)-treated 96-well plates (Corning) at a seeding density between 5,000–50,000 cells/well in a volume of 180 μL

Author Manuscript Author Manuscript Author Manuscript Author Manuscript

cell medium for 15–24 hours. The cells were treated in triplicate with 0.0086–128 nM of [^{77}Br]RD1 (122–500 MBq/μmol) with and without a blocking dose of 1 μM non-radioactive BrRD1. [^{77}Br]RD1 in PBS (BioWhittaker) was added to the wells in a volume of 20 μL for a total volume in wells of 200 μL for 2 hours.

A hemocytometer was used to verify the cell density per well at the time of contact in triplicate using wells with zero activity. The medium containing [^{77}Br]RD1 was removed and placed in corresponding polypropylene cluster tubes (Corning). The wells were rinsed with 100 μL of PBS and added to the same corresponding cluster tubes. The cells were then dispersed with 50 μL of 0.25% trypsin-EDTA (Corning) for 20 minutes at 5% CO_2 and 37°C and this volume collected. The wells were rinsed with 100 μL of PBS and collected in the same corresponding vial. The radioactivity in the cells+rinse and the medium+rinse was measured using a Wizard^2 Automatic Gamma Counter (PerkinElmer) calibrated by high purity germanium (HPGe) gamma spectroscopy (HPGe, Canberra C1519). Background and dead time were manually measured. For dead times higher than 10%, measurements were retaken after a period of decay. Cellular molar uptake (in attomol/cell) was calculated by dividing the cell-associated radioactivity (MBq) by the measured number of cells per well and the measured molar activity (MBq/nmol).

The total binding curve measured from the cells contacted with [^{77}Br]RD1 and the nonspecific binding curve measured from the cells contacted with [^{77}Br]RD1 + 1 μM BrRD1 were fitted using GraphPad Prism v9 (GraphPad Software, San Diego, CA, USA). The maximum number of binding sites per cell (B_{max}), equilibrium dissociation constant (K_d), and nonspecific binding slope (NS) were calculated (Eq. S1–S3).

2.4 Cytotoxicity following exposure to [^{77}Br]RD1

Cells were plated at a seeding density of 200 cells/well in 96-well white, opaque TC-treated plates (Falcon) for 2 hours before contact with varying concentrations of [^{77}Br]RD1 from 0.001–60 MBq/mL (0.0005–450 nM) for 7 days. Cell viability was assayed using Cell-Titer Glo 2.0 (Promega) by measuring adenosine triphosphate (ATP) with luminescence. Dose response curves were fitted using GraphPad Prism v9 and the half maximal effective concentrations (EC_{50}) were calculated as a function of molar concentration, activity concentration, and specific uptake using Equation S4. Radiation dose to the cell nucleus was calculated using Monte Carlo simulation with Medical Internal Radiation Dosimetry Cell (MIRDcell) v3.12, as previously described [51]. Further protocol details are provided in the supplementary methods.

2.5 PET/CT imaging and biodistribution of [^{76}Br]RD1

Imaging and biodistribution studies were approved by the Institutional Animal Care and Use Committee at the University of Wisconsin—Madison (IACUC M006459). Four female C57BL/6 mice (Jackson Laboratory, ME) aged 12 weeks were used for *in vivo* studies. Mice were imaged prone two at a time on an Inveon microPET/CT scanner (Siemens Medical Solutions) under anesthesia, with 1.5–3.5% isoflurane at a rate of 1–2 L/min of oxygen via nose cone after an induction with 3–5% isoflurane. X-ray computed tomography (CT) imaging lasted 10 minutes, followed by PET image acquisition. Mice received 5.1±0.1

Author Manuscript Author Manuscript Author Manuscript Author Manuscript

MBq of 23 MBq/nmol [^{76}Br]RD1 via tail vein (IV) injections at the beginning of a 1-h dynamic PET scan. Images were histogrammed into 1-minute bins between 1–5 minutes post injection (p.i.), 5-minute bins between 5–30 minutes p.i., and 10-minute bins between 30–60 minutes p.i. Static PET scans were performed at 4 h, 24 h, and 48 h p.i. and histogrammed into one frame (50 million counts/scan for all the time points except 20 million counts/scan at 48 h). PET images for static and dynamic scans were reconstructed using ordered-subset expectation maximization of 3 dimensions followed by the maximum a posteriori algorithm (18 iterations and 16 subsets). The corresponding CT was used for attenuation correction. PET/CT images were automatically coregistered and analyzed using Inveon Research Workplace 4.2 (Siemens Medical Solutions).

Regions of interest (ROIs) were drawn in the heart, lungs, brain, kidneys, bladder, liver, stomach, intestines, femur, and quadricep muscle. The mean percentage injected dose per volume (%ID/g) was measured after decay-correcting to time of injection. After the final PET/CT image at 48 h, mice were euthanized via CO_2 asphyxiation followed by exsanguination. The blood, heart, lungs, pancreas, spleen, kidneys, liver, gallbladder, large intestine, small intestine, stomach, femur bone, quadriceps muscle, and enteric (combined stomach and small and large intestine) contents were harvested and weighed. The radioactivity was measured using an automated HPGe-calibrated gamma counter (PerkinElmer). Measurements were background- and decay-corrected to time of injection to calculate the %ID/g. A partial volume (PV) correction phantom (Phantech, WI) with sphere volumes from 8–900 mm^3 filled with 142±6 kBq/mL of [^{76}Br]RD1 was PET imaged as described above, and the recovery coefficient (RC) curves were calculated.

2.6 [$^{76/77}$Br]RD1 three-dimensional dosimetry

PET/CT images were used to define the activity distribution and geometry for use in an in-house Monte Carlo (MC) dosimetry platform, RAPID [52]. PET/CT were coregistered and resampled in Amira (v5.3.3, Mercury Computer Systems, Berlin, Germany) and used to calculate the mean absorbed dose rate for each voxel after decay correction. This was done for each organ region at each timepoint. This was imported into the MC framework (Geant4, v9.6.p2) and the Auger electron function (ARMflag) was utilized for calculations using data from the Evaluated Atomic Data Library [53]. CT data were transformed from Hounsfield units into mass density using a CT scanner specific calibration curve. Evaluated Nuclear Structure Data Files (ENSDF, Brookhaven National Laboratory) data, which includes all MAe (>1 keV), β, and γ radiation emitted per decay, were used to calculate the source decay sampled uniformly in a voxel. The energy deposition was tracked to create a 3D cumulative dose distribution with the PET contours defining organ regions to calculate organ specific dose. To calculate the dose distribution for [^{77}Br]RD1, the PET images acquired with [^{76}Br]RD1 were corrected for physical decay differences between the two radionuclides.

The PET quantified [^{76}Br]RD1 organ %ID/g uptake in mice was used to estimate the human organ dose using OLINDA/EXM v1.1 [54] as described previously [55]. Briefly, the mouse biodistribution was assumed to be equal to human biodistribution. The mouse organ [^{76}Br]RD1 uptakes (%ID/g) were multiplied by the ratio of the average mouse mass in the study to the average human woman mass to get the estimated human organ %ID/g uptakes,

Author Manuscript Author Manuscript Author Manuscript Author Manuscript

which were multiplied by average human organ masses [56] to obtain organ-specific %ID in human. These values were used in OLINDA/EXM to calculate organ-level equivalent dose.

3. Statistical analysis

All data were obtained in technical and biological triplicate unless otherwise stated. Statistical analyses and nonlinear regression were performed using GraphPad Prism v9. Results are reported as mean ± standard deviation (SD) or with stated 95% confidence interval (CI).

4. Results

4.1 Radiosynthesis

The average cyclotron physical yield was 16±2 MBq·μA^{-1}·h^{-1} (n = 7) for ^{77}Br, 59±4 MBq·μA^{-1}·h^{-1} (n = 4) for ^{76}Br and the distillation yield was 67±13% (n=11). The non-decay corrected radiochemical yield (RCY) and molar activity (MA) for [^{77}Br]RD1 was 58±25% and 300±120 MBq/nmol (n = 7). The RCY and MA for [^{76}Br]RD1 was 5±3% and 23 MBq/nmol (n=2), respectively, when GBq-quantity [^{76}Br]bromide was stored in solution overnight prior to reaction. When stored dry, it was 73% and 740 MBq/nmol (n=1), respectively.

4.2 In vitro analysis

The total, nonspecific (Figure 2A–B) and specific (Figure 2C) binding were used to calculate the B_{max}, K_d and NS, which are summarized in Table 1. For the OVCAR8 PARP1-KO cell line, there was no statistical difference between the nonspecific and total binding measurements for molar concentrations above 25 nM (n = 4). This indicated a low number of specific binding sites that were small compared with the nonspecific binding above 25 nM. Thus, values measured above 25 nM were excluded from the B_{max}, K_d and NS fitting analysis for this cell line.

4.3 In vitro cytotoxicity

The cell survival curves of the various ovarian cancer cell lines are summarized in Figure 2D–F as a function of activity concentration (Figure 2D), molar concentration (Figure 2E and S3), and specific uptake (Figure 2F). The EC_{50} and the corresponding 95% confidence intervals (CI) are summarized in Table 2.

4.4 PET imaging, biodistribution, and dosimetry

Partial volume correction phantom results and recovery coefficient calibration curves are summarized in Figure S4. Significant [^{76}Br]RD1 uptake in the liver (brown arrow) occurred within 5 minutes p.i. and the gallbladder (blue arrow) between 1–4 hours p.i. (Figure 3A). The 48 h p.i. *in vivo* PET quantification was compared to the *ex vivo* biodistribution measurements (Figure 3B, Table S2). Time activity curves showed biphasic blood clearance with a calculated α-phase half-life of 1.5 min (95% CI: 1.2–1.9 min) and β-phase half-life of 85 min (95% CI: 67–107 min, Figure 3C). Based on the organ-averaged PET results from 1–48 h, 85±10% of [^{77}Br]RD1 was excreted from 1–24 hours and 69±15% of that remaining

Author Manuscript Author Manuscript Author Manuscript Author Manuscript

excreted from 24–48 hours. Dosimetry analyses of [$^{76/77}$Br]RD1 following injection in mice and humans are summarized in Figure 4 and Table S3.

5. Discussion

Radiopharmacological and toxicological properties of a PARP-targeted MAe emitting radiopharmaceutical [^{77}Br]RD1 were measured in ovarian cancer cell lines. [^{77}Br]RD1 demonstrated specific, blockable uptake with nanomolar binding affinity and attomoles of binding sites per cell. The binding affinity, represented by the equilibrium dissociation constant K_d, ranged from 6–30 nM with cell line variability potentially due to differences in relative expression levels of the various PARP isoforms. The number of specific binding sites per cell, represented by B_{max}, ranged from 0.8 – 11 amol/cell (0.5–6.6 million sites per cell). Radiotracer studies utilizing structurally analogous [^{125}I]KX1 have shown B_{max} to be strongly positively correlated to PARP1 expression, as determined by Western blot analysis [57]. Supporting this, the B_{max} of the OVCAR8 cell line (1.6 amol/cell) is a factor of two higher than the analogous PARP1 knock out cell line (0.83 amol/cell).

The EC_{50} (in nM) of [^{77}Br]RD1 was thousands of times lower compared to rucaparib for OVCAR8 (2,400x), OVCAR8 PARP1-KO (6,700x) and UWB1.289+BRCA1 (3,000x), and 70x lower for UWB1.289 [50]. These results show the radiotoxicity of [^{77}Br]RD1 is significantly greater than the chemotoxicity of structurally-related rucaparib in ovarian cancer. Compared to the radioiodinated MAe-emitting analog, [^{125}I]KX1, the EC_{50} (in MBq/mL) of [^{77}Br]RD1 is 5x and 4x higher for OVCAR8 and OVCAR8 PARP1-KO, respectively, and the D_{50} (Gy) is approximately 3x higher for OVCAR8 and OVCAR8 PARP1-KO, 1.7x higher for UWB1.289, and approximately the same for UWB1.289+BRCA1 [35]. This difference may be due to the smaller average number of MAes emitted with ^{77}Br (6–7 MAe/decay) compared with ^{125}I (~23 MAe/decay) [42]. When measured in terms of activity concentration, the OVCAR8 PARP1-KO cell line was significantly more [^{77}Br]RD1-tolerant (P=0.0140) compared to OVCAR8 (Figure 2D), with EC_{50} of 0.20 (95% CI: 0.15–0.28) MBq/mL and 0.070 (0.062–0.080) MBq/mL (Table 2), respectively. This agrees with Makvandi, et al. [57], which demonstrates that PARP expression is essential to the efficacy of MAe-emitting PARP inhibitors, where lower B_{max} values were associated with higher EC_{50} values. However, after accounting for the cell line's lower number of specific binding sites, this differential sensitivity was no longer observed (P=0.6228), with EC_{50} of 0.020 (0.015–0.027) Bq/cell and 0.018 (0.016–0.020) Bq/cell for OVCAR8 PARP1-KO and OVCAR8 cell lines, respectively (Figure 2F, Table 2). These results indicate that the PARP-expression dependence of [^{77}Br]RD1 radiotoxicity is driven by differences in specific binding site expression, in which the loss of PARP1 did not change the radiosensitivity of the cancer cell line.

[^{77}Br]RD1 had similar cytotoxic effects regardless of BRCA1 gene expression (Figure 2D–E). The chemotherapeutic effect of rucaparib and other PARP inhibitors results in increased cytotoxicity in homologous recombination deficient BRCA1 mutated cells [50], [58]. When adding the radiotherapeutic effect of the MAe emitting isotope ^{77}Br, this biomarker-dependency was no longer apparent—the [^{77}Br]RD1 showed similar cytotoxicity in UWB1.289 cells even with upregulated BRCA1 expression (Figure 2D–E) with EC_{50}

Author Manuscript Author Manuscript Author Manuscript Author Manuscript

values of 0.061 (0.044–0.086) MBq/mL and 0.068 (0.055–0.083) MBq/mL for UWB1.289 and UWB1.289+BRCA cell lines, respectively.

Hepatobiliary and renal excretion pathways were observed for [^{76}Br]RD1 (Figure 3A) in agreement with other radiolabeled PARP inhibitors [23], [36], [59], [60]. The excretion rate of [^{76}Br]RD1 (70–85% per day) was significantly faster than that of [^{82}Br]bromide (5% per day) [45], supporting the hypothesis that minimal debromination occurred *in vivo*. Future metabolite analyses are necessary to confirm this. Terminal *in vivo* and *ex vivo* biodistributions differed for organs with contents that were removed for *ex vivo* measurement, e.g., blood and enteric contents, and in organs with inhomogeneous radiopharmaceutical distribution, e.g., liver. At 48 h, [^{76}Br]RD1 resides mainly in the liver region. This prolonged retention of [^{77}Br]RD1 may cause toxicity in the liver, with dose estimates of 19.3 ± 0.3 mGy/MBq and 19 ± 2 mSv/GBq in mice and humans, respectively (Fig. 4, Table S3). The liver dose limit for external-beam radiotherapy is 30 Gy, which would limit the [^{77}Br]RD1 activity to approximately 1,600 GBq (Table S4). However, liver uptake of an olaparib-based fluorescent PARP inhibitor was observed to be cytoplasmic, significantly decreasing the equivalent dose to liver cell DNA compared to the nuclear uptake observed in tumor cells [27]. In mice, stomach and intestinal absorbed doses were 270 ± 30 and 720 ± 70 mGy/MBq, respectively, for [^{76}Br]RD1. However, as mentioned above, the *ex vivo* and *in vivo* differences indicate that most of the activity and thus dose is in the contents of the organ. Human dose estimates were compared to organ dose reported for ^{18}F-FTT [16]. All [^{76}Br]RD1 human equivalent organ dose estimates were 7 ± 2 times larger compared to PARP-targeted imaging agent, ^{18}F-FTT, except for lower large intestine (20 times larger). Dose limits for the reported organs [61] show that the dose limiting organ is the bone marrow, which limits [^{77}Br]RD1 injected activity to approximately 110 GBq.

6. Conclusion

The cytotoxicity of [^{77}Br]RD1 was found to be PARP expression dependent and BRCA1 status independent. These results together indicate the radiotherapeutic effect of the MAe emitting radionuclide is driving the cytotoxicity of [^{77}Br]RD1 beyond the PARP inhibitor chemotherapeutic effect. This study offers insights into the fundamental radiation biology of low energy electron emitting radiopharmaceuticals targeting the nuclear DNA damage response system. Future imaging and therapeutic studies should be conducted with further refined *in vivo* tumor models to show the efficacy of [^{76}Br]RD1 as a theranostic agent for ovarian cancer.

Supplementary Material

Refer to Web version on PubMed Central for supplementary material.

Acknowledgements

We thank the staff of the University of Wisconsin Carbone Cancer Center (UWCCC) Biostatistics Shared Resource for their valuable contributions to this research. We also thank the staff of the UWCCC Small Animal Imaging & Radiotherapy Facility for their technical support. Shared research services at the UWCCC are supported by Cancer Center Support Grant P30 CA014520.

Author Manuscript Author Manuscript Author Manuscript Author Manuscript

Funding

This research is supported by the U.S. Department of Energy Isotope Program, managed by the Office of Science for Isotope R&D and Production, grant number DE-SC0020960 and the U.S. Department of Defense Ovarian Cancer Research Program Pilot Award, grant number W81XWH2110351. J.C.M. is supported by the National Cancer Institute of the National Institutes of Health under Award Number T32CA009206. The project was supported by the Clinical and Translational Science Award (CTSA) program, through the NIH National Center for Advancing Translational Sciences (NCATS), grant UL1TR002373. B.P.B. is supported by NCI P01 CA250972-01 and NCI U01 CA233102-01. The content is solely the responsibility of the authors and does not necessarily represent the official views of the NIH.

10. References

[1]. Siegel RL, Miller KD, Wagle NS, and Jemal A, 'Cancer statistics, 2023.', CA Cancer J Clin, vol. 73, no. 1, pp. 17–48, Jan. 2023, doi: 10.3322/caac.21763. [PubMed: 36633525]

[2]. Jemal A, Thomas A, Murray T, and Thun M, 'Cancer Statistics, 2002', CA Cancer J Clin, vol. 52, no. 1, pp. 23–47, Jan. 2002, doi: 10.3322/canjclin.52.1.23. [PubMed: 11814064]

[3]. Marth C, Reimer D, and Zeimet AG, 'Front-line therapy of advanced epithelial ovarian cancer: standard treatment', Annals of Oncology, vol. 28, pp. viii36–viii39, Nov. 2017, doi: 10.1093/annonc/mdx450. [PubMed: 29232473]

[4]. Zhang C, Xu C, Gao X, and Yao Q, 'Platinum-based drugs for cancer therapy and anti-tumor strategies', Theranostics, vol. 12, no. 5, pp. 2115–2132, 2022, doi: 10.7150/thno.69424. [PubMed: 35265202]

[5]. Colombo PE, Fabbro M, Theillet C, Bibeau F, Rouanet P, and Ray-Coquard I, 'Sensitivity and resistance to treatment in the primary management of epithelial ovarian cancer', Crit Rev Oncol Hematol, vol. 89, no. 2, pp. 207–216, Feb. 2014, doi: 10.1016/j.critrevonc.2013.08.017. [PubMed: 24071502]

[6]. The Cancer Genome Atlas Research Network, 'Integrated genomic analyses of ovarian carcinoma', Nature, vol. 474, no. 7353, pp. 609–615, Jun. 2011, doi: 10.1038/nature10166. [PubMed: 21720365]

[7]. Ledermann JA, Drew Y, and Kristeleit RS, 'Homologous recombination deficiency and ovarian cancer', Eur J Cancer, vol. 60, pp. 49–58, Jun. 2016, doi: 10.1016/j.ejca.2016.03.005. [PubMed: 27065456]

[8]. Prakash R, Zhang Y, Feng W, and Jasin M, 'Homologous recombination and human health: The roles of BRCA1, BRCA2, and associated proteins', Cold Spring Harb Perspect Biol, vol. 7, no. 4, 2015, doi: 10.1101/cshperspect.a016600.

[9]. Lord CJ and Ashworth A, 'PARP inhibitors: Synthetic lethality in the clinic', Science (1979), vol. 355, pp. 1152–1158, 2017.

[10]. Yi M, Dong B, Qin S, Chu Q, Wu K, and Luo S, 'Advances and perspectives of PARP inhibitors', Exp Hematol Oncol, vol. 8, no. 29, pp. 1–12, Nov. 2019, doi: 10.1186/s40164-019-0154-9. [PubMed: 30622841]

[11]. Sonnenblick A, de Azambuja E, Azim HA Jr, and Piccart M, 'An update on PARP inhibitors —moving to the adjuvant setting', Nat Rev Clin Oncol, vol. 12, pp. 27–41, 2015. [PubMed: 25286972]

[12]. Lin Q et al. , 'PARP inhibitors as maintenance therapy in newly diagnosed advanced ovarian cancer: a meta-analysis', BJOG, vol. 128, no. 3, pp. 485–493, Feb. 2020, doi: 10.1111/1471-0528.16450. [PubMed: 32654312]

[13]. Zandarashvili L et al. , 'Structural basis for allosteric PARP-1 retention on DNA breaks', Science (1979), vol. 368, no. 6486, Apr. 2020, doi: 10.1126/SCIENCE.AAX6367.

[14]. Ambur Sankaranarayanan R, Kossatz S, Weber W, Beheshti M, Morgenroth A, and Mottaghy FM, 'Advancements in PARP1 targeted nuclear imaging and theranostic probes', J Clin Med, vol. 9, no. 7, 2020, doi: 10.3390/jcm9072130.

[15]. McDonald ES et al. , 'Positron emission tomography imaging of poly-(adenosine diphosphate-ribose) polymerase 1 expression in breast cancer: A nonrandomized clinical trial', JAMA Oncol, vol. 6, no. 6, pp. 921–923, Jun. 2020, doi: 10.1001/jamaoncol.2020.0334. [PubMed: 32297911]

Author Manuscript Author Manuscript Author Manuscript Author Manuscript

[16]. Michel LS et al. , 'PET of poly (ADP-ribose) polymerase activity in cancer: Preclinical assessment and first in-human studies', Radiology, vol. 282, no. 2, pp. 453–463, Mar. 2017, doi: 10.1148/radiol.2016161929. [PubMed: 27841728]

[17]. Young RJ et al. , 'Preclinical and first-in-human-brain-cancer applications of [18F]poly (ADP-ribose) polymerase inhibitor PET/MR', Neurooncol Adv, vol. 2, no. 1, Jan. 2020, doi: 10.1093/noajnl/vdaa119.

[18]. Puentes LN, Makvandi M, and Mach RH, 'Molecular imaging: PARP-1 and beyond', Journal of Nuclear Medicine, vol. 62, no. 6, pp. 765–770, Jun. 2021, doi: 10.2967/jnumed.120.243287. [PubMed: 33579802]

[19]. McDonald ES et al. , 'In vivo visualization of PARP inhibitor pharmacodynamics', JCI Insight, vol. 6, no. 8, Apr. 2021, doi: 10.1172/jci.insight.146592.

[20]. Carney B et al. , 'Non-invasive PET imaging of PARP1 expression in glioblastoma models', Mol Imaging Biol, vol. 18, no. 3, pp. 386–392, Jun. 2016, doi: 10.1007/s11307-015-0904-y. [PubMed: 26493053]

[21]. Chan CY, Tan KV, and Cornelissen B, 'PARP inhibitors in cancer diagnosis and therapy', Clinical Cancer Research, vol. 27, no. 6, pp. 1585–1594, Mar. 2021, doi: 10.1158/1078-0432.CCR-20-2766. [PubMed: 33082213]

[22]. Chen Z, Destro G, Guibbal F, Chan CY, Cornelissen B, and Gouverneur V, 'Copper-Mediated Radiosynthesis of [18F]Rucaparib', Org Lett, vol. 23, no. 18, pp. 7290–7294, Sep. 2021, doi: 10.1021/acs.orglett.1c02770. [PubMed: 34459606]

[23]. Chan CY et al. , 'Imaging PARP with [18F]rucaparib in pancreatic cancer models', Eur J Nucl Med Mol Imaging, vol. 49, no. 11, pp. 3668–3678, 2022, doi: 10.1007/s00259-022-05835-4. [PubMed: 35614267]

[24]. Bowden GD et al. , 'DoE Optimization Empowers the Automated Preparation of Enantiomerically Pure [18F]Talazoparib and its In Vivo Evaluation as a PARP Radiotracer', J Med Chem, vol. 64, no. 21, pp. 15690–15701, Nov. 2021, doi: 10.1021/acs.jmedchem.1c00903. [PubMed: 34672571]

[25]. Zhou D et al. , 'Radiosynthesis and Evaluation of Talazoparib and Its Derivatives as PARP-1-Targeting Agents', Biomedicines, vol. 9, no. 5, 2021, doi: 10.3390/biomedicines9050565.

[26]. Wilson TC et al. , 'PET Imaging of PARP Expression Using 18F-Olaparib', Journal of Nuclear Medicine, vol. 60, no. 4, p. 504, Apr. 2019, doi: 10.2967/jnumed.118.213223. [PubMed: 30389822]

[27]. Guibbal F et al. , 'Manual and automated Cu-mediated radiosynthesis of the PARP inhibitor [18F]olaparib', Nat Protoc, vol. 15, no. 4, pp. 1525–1541, 2020, doi: 10.1038/s41596-020-0295-7. [PubMed: 32111986]

[28]. Jannetti SA et al. , 'PARP-1-targeted radiotherapy in mouse models of glioblastoma', Journal of Nuclear Medicine, vol. 59, no. 8, pp. 1225–1233, Aug. 2018, doi: 10.2967/jnumed.117.205054. [PubMed: 29572254]

[29]. Makvandi M et al. , 'Targeting PARP-1 with Alpha-Particles Is Potently Cytotoxic to Human Neuroblastoma in Preclinical Models', Mol Cancer Ther, vol. 18, no. 7, pp. 1195–1204, Jul. 2019, doi: 10.1158/1535-7163.MCT-18-0837. [PubMed: 31072830]

[30]. Dabagian H et al. , 'PARP Targeted Alpha-Particle Therapy Enhances Response to PD-1 Immune-Checkpoint Blockade in a Syngeneic Mouse Model of Glioblastoma', ACS Pharmacol Transl Sci, vol. 4, no. 1, pp. 344–351, Feb. 2021, doi: 10.1021/acsptsci.0c00206. [PubMed: 33615184]

[31]. Makvandi M et al. , 'Pre-clinical investigation of astatine-211-parthanatine for high-risk neuroblastoma', Commun Biol, vol. 5, no. 1, p. 1260, 2022, doi: 10.1038/s42003-022-04209-8. [PubMed: 36396952]

[32]. Lee H et al. , 'PARP-1-Targeted auger emitters display high-LET cytotoxic properties in vitro but show limited therapeutic utility in solid tumor models of human neuroblastoma', Journal of Nuclear Medicine, vol. 61, no. 6, pp. 850–856, Jun. 2020, doi: 10.2967/jnumed.119.233965. [PubMed: 31676730]

Author Manuscript Author Manuscript Author Manuscript Author Manuscript

[33]. Wilson T et al. , 'PARP-Targeted Auger Therapy in p53 Mutant Colon Cancer Xenograft Mouse Models', Mol Pharm, vol. 18, no. 9, pp. 3418–3428, Sep. 2021, doi: 10.1021/acs.molpharmaceut.1c00323. [PubMed: 34318678]

[34]. Sankaranarayanan RA et al. , 'Auger Emitter Conjugated PARP Inhibitor for Therapy in Triple Negative Breast Cancers: A Comparative In-Vitro Study', Cancers (Basel), vol. 14, no. 1, Jan. 2022, doi: 10.3390/cancers14010230.

[35]. Riad A et al. , 'PARP Theranostic Auger Emitters Are Cytotoxic in BRCA Mutant Ovarian Cancer and Viable Tumors from Ovarian Cancer Patients Enable Ex-Vivo Screening of Tumor Response', Molecules, vol. 25, no. 24, Dec. 2020, doi: 10.3390/MOLECULES25246029.

[36]. Sreekumar S et al. , 'Preclinical efficacy of a PARP-1 targeted Auger-emitting radionuclide in prostate cancer', Int J Mol Sci, vol. 24, 2022.

[37]. Pirovano G et al. , 'Targeted brain tumor radiotherapy using an auger emitter', Clinical Cancer Research, vol. 26, no. 12, pp. 2871–2881, Jun. 2020, doi: 10.1158/1078-0432.CCR-19-2440. [PubMed: 32066626]

[38]. Salinas B et al. , 'Radioiodinated PARP1 tracers for glioblastoma imaging', EJNMMI Res, vol. 5, no. 1, p. 46, 2015, doi: 10.1186/s13550-015-0123-1. [PubMed: 26337803]

[39]. Ku A, Facca VJ, Cai Z, and Reilly RM, 'Auger electrons for cancer therapy – a review', EJNMMI Radiopharm Chem, vol. 4, no. 1, Dec. 2019, doi: 10.1186/s41181-019-0075-2.

[40]. Destro G et al. , 'A radioiodinated rucaparib analogue as an Auger electron emitter for cancer therapy', Nucl Med Biol, vol. 116–117, p. 108312, Jan. 2023, doi: 10.1016/j.nucmedbio.2022.108312.

[41]. Syed YY, 'Rucaparib: First Global Approval', Drugs, vol. 77, no. 5, pp. 585–592, Apr. 2017, doi: 10.1007/s40265-017-0716-2. [PubMed: 28247266]

[42]. Eckerman K and Endo A, 'Nuclear decay data for dosimetric calculations. ICRP Publication 107', Annals ICRP, vol. 38, no. 3, pp. 1–123, 2008.

[43]. Cornelissen B and Vallis KA, 'Targeting the nucleus: An overview of Auger-electron radionuclide therapy', Curr Drug Discov Technol, vol. 7, p. 263, 2010. [PubMed: 21034408]

[44]. Rowland DJ, McCarthy TJ, and Welch MJ, 'Radiobromine for Imaging and Therapy', in Handbook of Radiopharmaceuticals, John Wiley & Sons, Ltd, 2005, pp. 441–465. doi: 10.1002/0470846380.ch14.

[45]. Pavelka S, Babický A, Vobecký M, Lener J, and Švandová E, 'Bromide kinetics and distribution in the rat. I.', Biol Trace Elem Res, vol. 76, pp. 57–66, 2000, doi: 10.1385/BTER:76:1:57. [PubMed: 10999430]

[46]. Ribeiro MJ et al. , 'Comparison of fluorine-18 and bromine-76 imaging in positron emission tomography', Eur J Nucl Med, vol. 26, no. 7, 1999.

[47]. Welch MJ and Mcelvany KD, 'Radionuclides of bromine for use in biomedical studies', Radiochim Acta, vol. 34, pp. 41–46, 1983.

[48]. Ellison PA et al. , 'Improved production of 76Br, 77Br and 80mBr via CoSe cyclotron targets and vertical dry distillation', Nucl Med Biol, vol. 80–81, pp. 32–36, 2020, doi: 10.1016/j.nucmedbio.2019.09.001.

[49]. Mixdorf JC, Hoffman SLV, Aluicio-Sarduy E, Barnhart TE, Engle JW, and Ellison PA, 'Copper-mediated radiobromination of (hetero)aryl boronic pinacol esters', Journal of Organic Chemistry, no. 88, pp. 2089–2094, Feb. 2023, doi: 10.1021/acs.joc.2c02420. [PubMed: 36745853]

[50]. Makvandi M et al. , 'A PET imaging agent for evaluating PARP-1 expression in ovarian cancer', Journal of Clinical Investigation, vol. 128, no. 5, pp. 2116–2126, May 2018, doi: 10.1172/JCI97992. [PubMed: 29509546]

[51]. Vaziri B et al. , 'MIRD pamphlet No. 25: MIRDcell V2.0 software tool for dosimetric analysis of biologic response of multicellular populations', Journal of Nuclear Medicine, vol. 55, no. 9, pp. 1557–1564, Sep. 2014, doi: 10.2967/jnumed.113.131037. [PubMed: 25012457]

[52]. Besemer AE, Yang YM, Grudzinski JJ, Hall LT, and Bednarz BP, 'Development and validation of RAPID: A patient-specific Monte Carlo three-dimensional internal dosimetry platform', Cancer Biother Radiopharm, vol. 33, no. 4, pp. 155–165, May 2018, doi: 10.1089/cbr.2018.2451. [PubMed: 29694246]

Author Manuscript Author Manuscript Author Manuscript Author Manuscript

[53]. Perkins ST, Cullen DE, Chen MH, Rathkopf J, Scofield J, and Hubbell JH, 'Tables and graphs of atomic subshell and relaxation data derived from the LLNL Evaluated Atomic Data Library (EADL), Z = 1−-100', United States, 1991. doi: 10.2172/10121422.

[54]. Stabin MG, Sparks RB, and Crowe E, 'OLINDA/EXM: The Second-Generation Personal Computer Software for Internal Dose Assessment in Nuclear Medicine', Journal of Nuclear Medicine, vol. 46, no. 6, p. 1023, Jun. 2005, [Online]. Available: http://jnm.snmjournals.org/content/46/6/1023.abstract [PubMed: 15937315]

[55]. Marsh IR et al. , 'Preclinical pharmacokinetics and dosimetry studies of 124I/131I-CLR1404 for treatment of pediatric solid tumors in murine xenograft models', Journal of Nuclear Medicine, vol. 60, no. 10, pp. 1414–1420, Oct. 2019, doi: 10.2967/jnumed.118.225409. [PubMed: 30926646]

[56]. Valentin J, 'Basic anatomical and physiological data for use in radiological protection: reference values: ICRP Publication 89', Ann ICRP, vol. 32, no. 3, pp. 1–277, 2002, doi: 10.1016/S0146-6453(03)00002-2.

[57]. Makvandi M et al. , 'A radiotracer strategy to quantify PARP-1 expression in vivo provides a biomarker that can enable patient selection for PARP inhibitor therapy', Cancer Res, vol. 76, no. 15, pp. 4516–4524, Aug. 2016, doi: 10.1158/0008-5472.CAN-16-0416. [PubMed: 27261505]

[58]. Makvandi M et al. , 'A radiotracer strategy to quantify PARP-1 expression in vivo provides a biomarker that can enable patient selection for PARP inhibitor therapy', Cancer Res, vol. 76, no. 15, pp. 4516–4524, Aug. 2016, doi: 10.1158/0008-5472.CAN-16-0416. [PubMed: 27261505]

[59]. Zhou D et al. , 'Synthesis, [18F] radiolabeling, and evaluation of poly (ADP-ribose) polymerase-1 (PARP-1) inhibitors for in vivo imaging of PARP-1 using positron emission tomography', Bioorg Med Chem, vol. 22, no. 5, pp. 1700–1707, Mar. 2014, doi: 10.1016/j.bmc.2014.01.019. [PubMed: 24503274]

[60]. Zhou D et al. , 'Preliminary evaluation of a novel 18F-labeled PARP-1 ligand for PET imaging of PARP-1 expression in prostate cancer', Nucl Med Biol, vol. 66, pp. 26–31, 2018, doi: 10.1016/j.nucmedbio.2018.08.003. [PubMed: 30195072]

[61]. Wahl RL et al. , 'Normal-Tissue Tolerance to Radiopharmaceutical Therapies, the Knowns and the Unknowns', Journal of Nuclear Medicine, vol. 62, no. Supplement 3, p. 23S, Dec. 2021, doi: 10.2967/jnumed.121.262751. [PubMed: 34857619]

Author Manuscript Author Manuscript Author Manuscript Author Manuscript

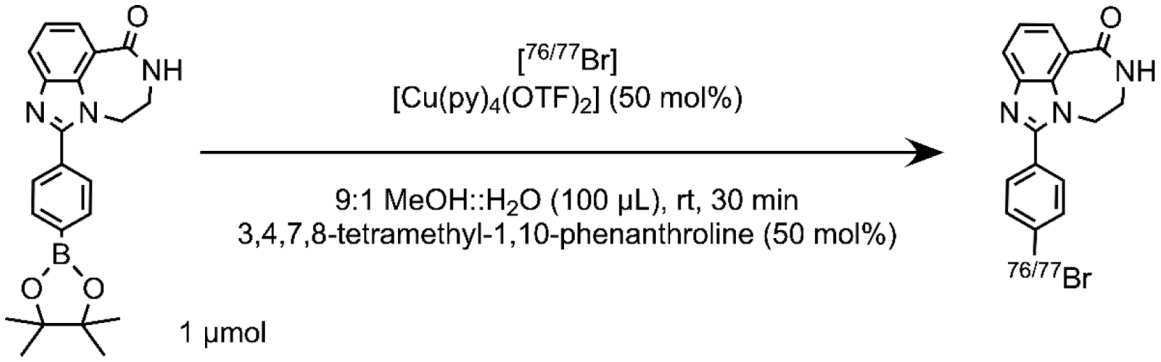

Figure 1:
Radiosynthesis of $^{76/77}$Br-labeled PARP1 inhibitor [$^{76/77}$Br]RD1.

Author Manuscript
Author Manuscript
Author Manuscript
Author Manuscript

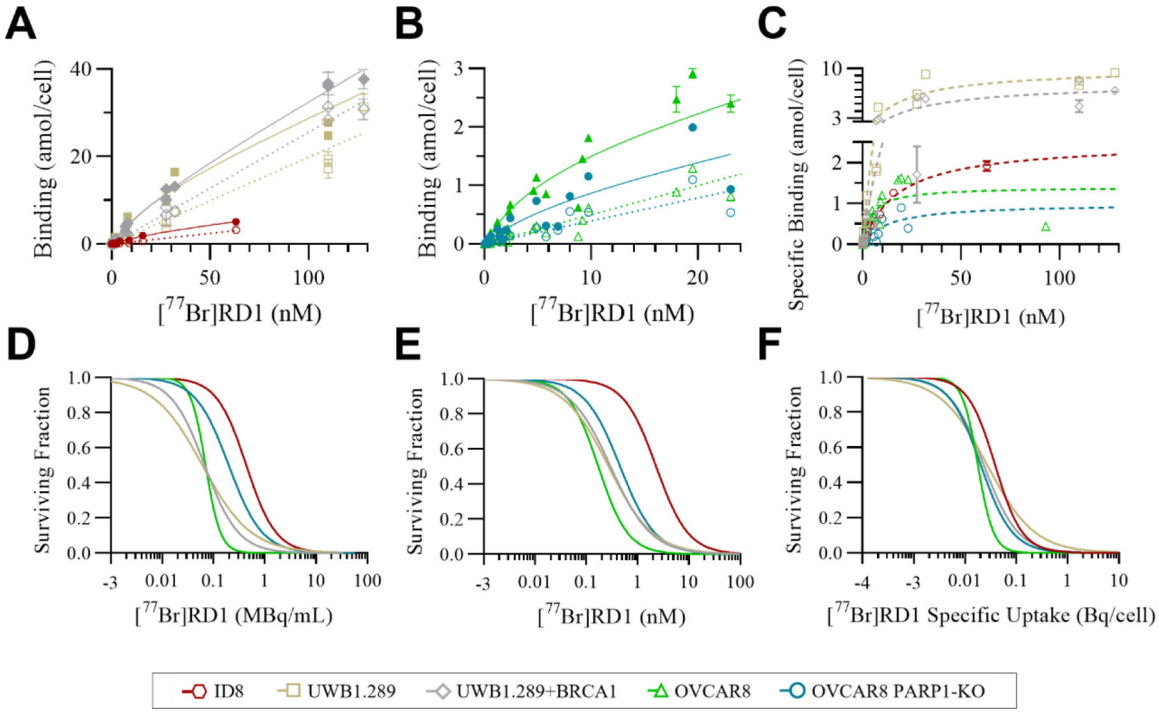

Figure 2:

Total (closed symbols, solid lines) and nonspecific (open symbols, dotted lines) binding of (A) UWB1.289 (gold, n=3), UWB1.289 +BRCA1 (gray, n=3), ID8 (red, n=2) (B) OVCAR8 (green, n=4), and OVCAR8 PARP1-KO (blue, n=4) and (C) the specific binding (dashed lines) of [^{77}Br]RD1 as a function of radiopharmaceutical molar concentration. (D) The cell survival of the same cell lines as a function of radiopharmaceutical activity concentration, (E) molar concentration, and (F) specific uptake (Bq/cell) inherent to the cell lines.

Author Manuscript Author Manuscript Author Manuscript Author Manuscript

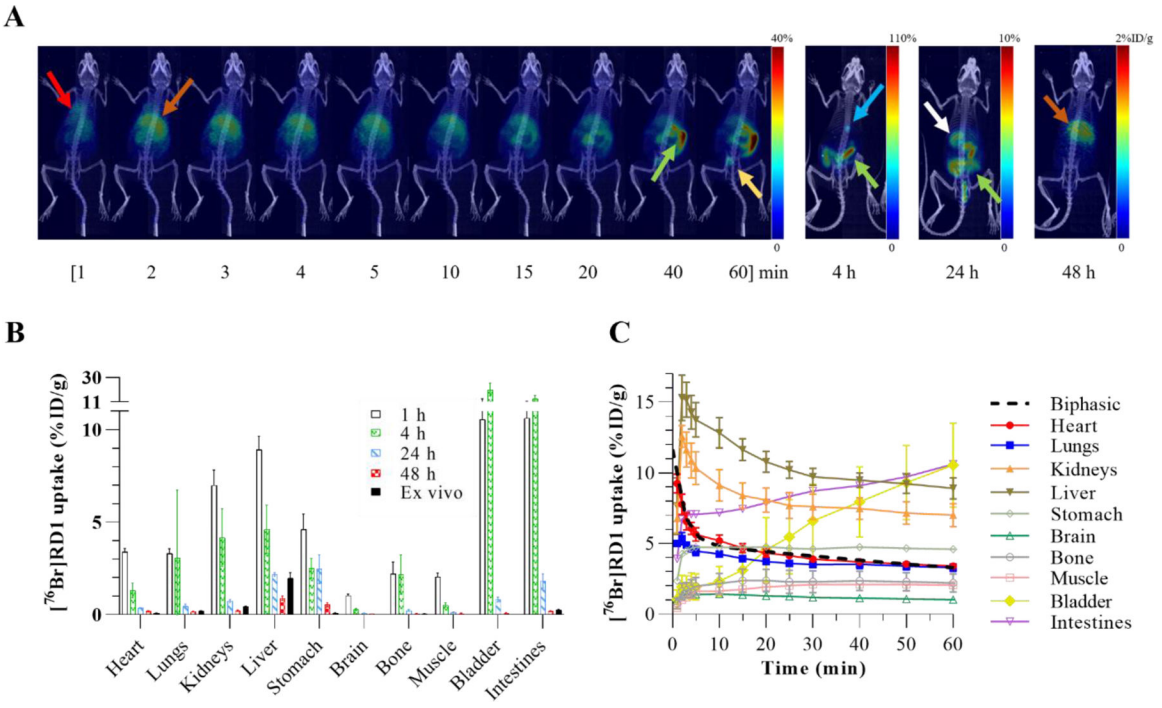

Figure 3:

(A) PET maximum intensity projection (MIP) images of a representative mouse injected intravenously with [^{76}Br]RD1. Red arrow: heart; brown arrow: liver; green arrow: intestines; yellow arrow: bladder; blue arrow: gallbladder; white arrow: stomach contents. (B) A comparison between the *in vivo* measurements at four time points p.i. and the *ex vivo* measurements (n=4). *Ex vivo* intestinal uptake was the average measurement of the small intestine, large intestine, and enteric contents. (C) Time activity curves based on ROI analysis of dynamic PET images.

Author Manuscript Author Manuscript Author Manuscript Author Manuscript

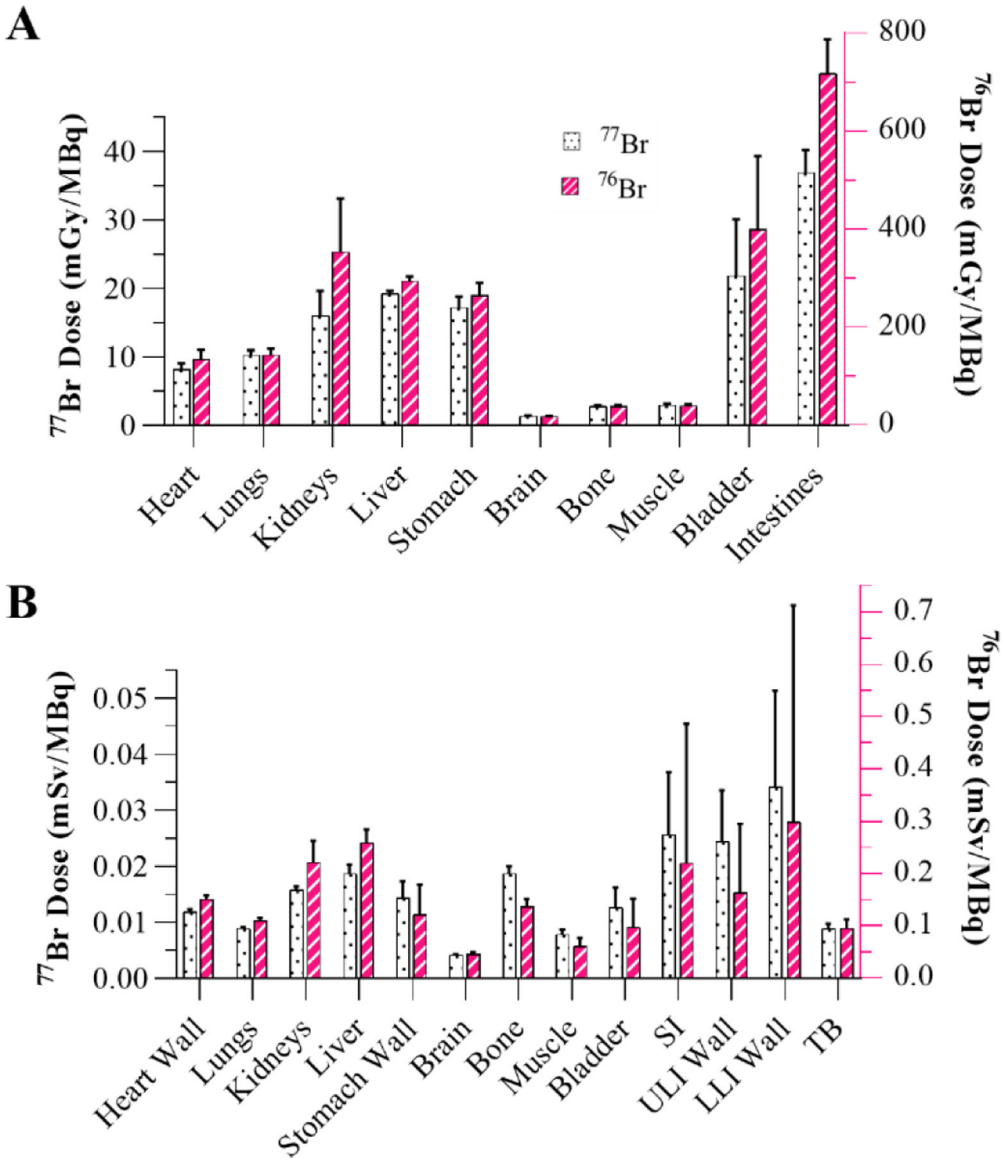

Figure 4:

Dosimetry analysis showing (A) organ-level absorbed dose following [$^{76/77}$Br]RD1 administration in mice using RAPID and (B) equivalent dose in female humans using OLINDA. SI: small intestine; ULI: upper large intestine; LLI: lower large intestine; TB: total body.

Author Manuscript

Author Manuscript

Author Manuscript

Author Manuscript

Table 1:

The [^{77}Br]RD1 pharmacological parameters calculated from total and nonspecific binding studies in the various ovarian cancer cell lines and their corresponding 95% CI.

Ovarian Cancer Cell Line	B_{max} **(95% CI) (attomol/cell)**	K_d**(95% CI) (nM)**	**NS (95% CI) (attomol/cell/nM)**
ID8	3.0 (2.4–3.9)	31 (20–49)	0.049 (0.047–0.052)
OVCAR8	1.6 (1.4–1.8)	6.0 (4.2–8.2)	0.050 (0.048–0.052)
OVCAR8 PARP1-KO	0.83 (0.50–1.5)	7.5 (2.7–20)	0.039 (0.033–0.046)
UWB1.289	11 (7.9–16)	24 (10–57)	0.20 (0.19–0.21)
UWB1.289+BRCA1	8.6 (6.6–11)	25 (13–48)	0.26 (0.25–0.26)

Author Manuscript

Author Manuscript

Author Manuscript

Author Manuscript

Table 2:

The [^{77}Br]RD1 toxicological EC_{50} values of the various ovarian cancer cell lines and their corresponding 95% CI.

Ovarian Cancer Cell Line	Molar Concentration (nM) EC_{50} 95% CI	Activity Concentration (10^{-2} MBq/mL) EC_{50} 95% CI	Cellular Activity Uptake (10^{-2} Bq/cell) EC_{50} 95% CI	Nuclear Dose (Gy) D_{50}
ID8	2.3 (1.8–2.9)	44 (36–53)	3.9 (3.3–4.6)	9.2±1.0
OVCAR8	0.17 (0.13–0.24)	7.0 (6.2–8.0)	1.8 (1.6–2.0)	4.3±0.3
OVCAR8 PARP1-KO	0.46 (0.34–0.62)	20 (15–28)	2.0 (1.5–2.7)	3.4±0.6
UWB1.289	0.27 (0.21–0.36)	6.1 (4.4–8.6)	2.7 (2.0–3.7)	3.9±0.8
UWB1.289+BRCA1	0.30 (0.22–0.41)	6.8 (5.5–8.3)	2.3 (1.9–2.8)	3.3±0.4